

# FEASIBILITY FOR IMPROVING AMBIENT TEMPERATURE TOUGHNESS OF MOSI<sub>2</sub> AND ITS COMPOSITES

Final Report  
Grant No. N000149410553

A. Newman\*, S. Sampath,<sup>†</sup> and H. Herman<sup>†</sup>  
Department of Materials Science and Engineering  
State University of New York  
Stony Brook, NY 11794-2275  
Tel: (516)-632-8515, Fax: (516)-632-8052

## ABSTRACT

Due to its high melting point and oxidation resistance, molybdenum disilicide (MoSi<sub>2</sub>) is a candidate for high temperature structural components. However, in order for MoSi<sub>2</sub> to be applicable for these applications, the high temperature creep resistance and low temperature fracture toughness of the compound need to be substantially improved. In this ONR-sponsored study, we are examining the effects of processing on the resulting microstructure and properties of reinforced and unreinforced MoSi<sub>2</sub>. Samples have been obtained from several laboratories with the goal of determining the effects of purity and processing. The results indicate that a finer grain size in combination with the addition of small particles, whether silica, SiC, or precipitates, contributes to the improvement in the material's low temperature fracture toughness.

## INTRODUCTION

MoSi<sub>2</sub>-based composites have been considered for high temperature structural applications due to the material's high melting point (2030°C), excellent oxidation resistance, electro-discharge machinability, and stability with compositing agents.<sup>1,2</sup> These silicide-based materials possess enhanced reliability and manufacturability as well as reduced cost over the present generation of structural ceramics.<sup>3</sup> The material is ductile at high temperatures, offering potential opportunities for hot forming operations. MoSi<sub>2</sub> has excellent high temperature oxidation resistance, having traditionally been employed as a heating element in air furnaces up to 1700°C.

For the silicides to become commercially viable as high temperature structural materials, two important issues must be addressed: (1) lack of ductility at ambient temperatures, and (2) poor tensile creep resistance at high temperatures.

A number of processing approaches are employed to fabricate monolithic and composite MoSi<sub>2</sub>. Included among these are hot pressing,<sup>4</sup> hot isostatic pressing,<sup>5</sup> self-propagating high temperature synthesis,<sup>6</sup> and plasma spray forming.<sup>7</sup> Recent developments based on alloying and compositing strategies indicate potential for improving these properties, however, numerous issues relative to processing-structure-property relationships remain unresolved. Due to variations in composition and impurity content, as well as processing and testing protocols, a direct comparison of mechanical properties is difficult, especially with respect to fracture toughness values. Indentation fracture toughness measurements reported in the literature show considerable variability from 2.3 to 5.9 MPam<sup>1/2</sup> for MoSi<sub>2</sub><sup>8-13</sup> and from 3 to 7.5 MPam<sup>1/2</sup> for its

\* Graduate Student

<sup>†</sup> Co-Primary Investigators

DISTRIBUTION STATEMENT A

Approved for public release;  
Distribution Unlimited

19970610 037

composites.<sup>8-10,12,14</sup> It is important to note that four-point bend and short rod tests generally give a lower fracture toughness value than indentation measurements.<sup>3</sup>

While MoSi<sub>2</sub> is brittle at room temperature, it exhibits dislocation plasticity at high temperatures. An early examination reported the ductile-to-brittle transition temperature (DBTT) for MoSi<sub>2</sub> to be about 1000°C.<sup>15</sup> However, recent examinations of the DBTT, using very low silica samples, have identified the transition point to be between 1300°C and 1400°C.<sup>16,17</sup> Investigators studying single crystal MoSi<sub>2</sub> recently observed slip for several crystal orientations at temperatures as low as ~173°K.<sup>18</sup>

MoSi<sub>2</sub> fabricated using powder processing procedures will have an intrinsic amount of silica, because of the high reactivity of silicon with oxygen.<sup>19</sup> The presence of silica as particles or as a thin film grain boundary phase can influence fracture behavior. There are conflicting observations in the literature with regard to the morphology and distribution of intrinsic silica in polycrystalline MoSi<sub>2</sub>. *In situ* Auger analysis of a 10-20 micron grain size sample that fractures intergranularly with silica particles within and at grain boundaries, indicates no oxygen enrichment at the grain boundary surface.<sup>20</sup> Chou *et al.* have indicated the possibility that low-angle grain boundaries may be impervious to oxygen diffusion.<sup>21</sup> However, conflicting TEM observation reported by S. Maloy *et al.* indicates a silaceous grain boundary phase.<sup>22</sup>

The influence of the silica grain boundary phase can be avoided by examining the properties of single crystal MoSi<sub>2</sub>. Single crystal MoSi<sub>2</sub> displays plastic behavior at room temperature in some orientations. Some early single crystal work demonstrated that slip is observed at ambient temperature by the observation of slip lines around Knoop and Vickers indentations.<sup>23</sup> Embury *et al.* examined the plastic deformation zone surrounding an indentation by TEM and observed dislocation networks and prismatic punches.<sup>24</sup> Slip systems were determined by examining the surface slip traces on a sample deformed in compression.<sup>25</sup> The [001]-oriented single crystal does not plastically deform at temperatures below 1300°C. Other orientations are more promising with three slip systems active at ambient temperatures, {110}<111], {011}<100], and {013}<331]. Two other slip systems, {010}<100] and {023}<100], are operative at higher temperatures. The above mentioned slip systems are operative, but the primary problem before satisfying von Mises' ductility criteria is the critical-resolved-shear-stress anisotropy.

Having only limited success with single crystal MoSi<sub>2</sub>, approaches to improve the low-temperature toughness and high temperature creep properties of MoSi<sub>2</sub> have been based primarily on compositing and secondarily on alloying. The compositing strategies include additions of whiskers or particulates of SiC, ZrO<sub>2</sub>, Si<sub>3</sub>N<sub>4</sub>,<sup>26</sup> SiC-Si<sub>3</sub>N<sub>4</sub><sup>27</sup> and ductile fibers, such as Nb. The composite studies have shown considerable promise, especially in the area of creep resistance.

Aiken reported that ambient temperature plasticity is improved by reinforcement with micron-sized particles.<sup>28</sup> However, it is not clear whether the improvement in plasticity, hence toughness, is the result of a greater propensity for microcracking or actual plastic deformation.<sup>28</sup> Samples from the present study have silica particles that are within that size regime. Petrovic *et al.* observed that dislocations and microcracks around zirconia particles are produced during processing, but the mechanism for the apparent enhanced fracture toughness was believed to be microcracking.<sup>29</sup> Gibala *et al.* has observed softening in thin film zirconia - MoSi<sub>2</sub> and dispersoid TiC - MoSi<sub>2</sub> systems at ambient temperatures.<sup>30</sup>

In order to improve the low-temperature toughness and high temperature creep properties of MoSi<sub>2</sub>, numerous approaches, primarily based on compositing have been proposed. The

compositing schemes include additions of whiskers or particulates of SiC, ZrO<sub>2</sub>, and ductile fibers, such as Nb. The results of the composite studies have shown considerable promise, especially in the area of creep resistance.

As an alternative to, or in conjunction with compositing, microalloying or macroalloying (> 1 wt% alloy addition) has been suggested as a means of improving the mechanical properties.<sup>31,32</sup> Yamaguchi *et al.*<sup>33</sup> have indicated that additions of Cr, Ta, V and Nb may destabilize the C11b structure with respect to the C40 structure. A three atomic percent substitution with Cr in a single crystal produced only minimal compressive ductility at 900-1500°C.<sup>34</sup> Recent work by Stergiou and Tsakiroopoulos<sup>35</sup> has reported lower hardness values with additions of W, Ta, and Al. W forms a solid solution with MoSi<sub>2</sub> in the C11b crystal structure and suppresses the formation of Mo<sub>5</sub>Si<sub>3</sub>. Ta additions result in a lamellar microstructure consisting of the C11b and C40 structures which also suppresses Mo<sub>5</sub>Si<sub>3</sub> formation. Al additions lead to the formation of the C40 and C54 structures. In other recent work, Si atom substitutions in the MoSi<sub>2</sub> lattice with Al, B, and Ge and molybdenum atom substitutions with Hf, Nb, and Re did not result in any effective toughness improvements. The DBTTs remained in the range of 1250°C to 1350°C.<sup>36</sup> Alloying with Re showed lowering of hardness and improving pest resistance, but no improvement in fracture toughness was observed.<sup>37</sup>

The purpose of this ONR investigation was to examine the room temperature mechanical properties of unreinforced MoSi<sub>2</sub> with respect to purity, grain size, and porosity. The principal objective was to determine the role of these variables on fracture toughness, which will yield alloy development and processing methods with which to enhance the intrinsic fracture toughness of MoSi<sub>2</sub>. It is envisioned that such an approach, in combination with appropriate compositing strategies, has the potential for producing material systems with enhanced fracture toughness (> 10 MPam<sup>1/2</sup>), while maintaining acceptable creep resistance.

### EXPERIMENTAL PROCEDURE

Samples produced by various processing methods, were obtained from several laboratories. The microstructures of these samples are presented in Figure 1. Knoop and Vickers indentations with loads of 1 kg or less were performed using a Buehler Micromet II Microhardness Tester. Additional Vickers indentations of 3 and 10 kg were obtained using a Rockwell Hardness Tester. Acoustic emissions (AE) were monitored on several of the Vickers 1 kg indentations. The resultant acoustic signal was transmitted to a Hartford Steam Boiler Inspection Technologies AET5500 analyzer with a transducer having a 175 KHz resonant frequency. The signal was subjected to a preamplifier filter with a 125 to 1000 KHz range and a threshold voltage of 0.4. The amplitude, rise time, and the event's duration were logged for each AE event. Nanoindentations were performed using a Nanoindenter<sup>®</sup> (Nanoindenter is a registered trademark of Nano Instruments, Inc., Knoxville, TN) at the Oak Ridge National Laboratory. The system has load and displacement resolutions of 0.3 µN and 0.16 nm, respectively. Methods of analyzing the hardness and elastic modulus from the load - displacement curves are reported in the literature.<sup>38</sup>

Oxygen analysis was performed on a Leco TC-136 analyzer using 5 runs for each sample. The grain size was measured manually using the linear intercept method. Density of the samples was determined by the water immersion method. Oxidation studies were performed at 500°C for 300 hours, under flowing air with a room temperature relative humidity of 23-35%. The amount of oxide growth and phase composition was determined by X-ray diffraction (XRD).

Vickers indentation crack measurements were employed to calculate fracture toughness values. An initial comparison is based on the Lawn-Evans crack model by measuring the longest crack distance from the corners of the indent. Fracture toughness is then obtained from the Anstis equation,  $K_{Ic} = 0.016(E/H)^{1/2}P/c^{3/2}$ , where  $P$  is the load and  $c$  is the crack length.<sup>39</sup> A more general analysis for comparison purposes of cracking behavior and toughening mechanisms in  $MoSi_2$  is based on measuring the crack length: the longest traveling crack from the center of the indent, irrespective of whether the crack meets with the corners of the indent. Further, the hardness-to-modulus ratio,  $H/E$ , is determined for each sample and included in the latter analysis to improve the accuracy of determining the material's fracture toughness.

## RESULTS AND DISCUSSION

### *Effect of purity and processing on the microstructure and oxidation*

Table I and Table II summarize the various  $MoSi_2$  samples, their processing methods, and microstructural features. Samples have been obtained from various laboratories and this has provided the diversity of specimens needed to examine the differences in purity, grain size and porosity, which result from differences in parent materials and processing methods. The present approach enables normalization of the results and allows for a uniform comparison of microstructure and the resulting properties.

Table I. Sample Processing Methods and Microstructure Characteristics

Sample Code	Processing	Grain Size ( $\mu m$ )	Oxygen (wt%)
VPS2	vacuum plasma spraying, as-sprayed <sup>40</sup>	1.0-3.0	4.4
VPS1	vacuum plasma spraying, 24 hrs at 1100°C <sup>7</sup>	1.0-3.0	N/A
SHS	reaction synthesis, hot pressing 1600°C <sup>6</sup>	3.9	2.6
HIP1	hot isostatic pressing at 1350°C, 170 MPa <sup>41</sup>	4.3	6.3
HIP2	hot isostatic pressing <sup>42</sup>	8.3	0.97
HP1	hot pressing at 1600°C <sup>31,32</sup>	24.2	1.5
EHIP	elemental powders, hot isostatic pressing at 1400°C, 200 MPa <sup>5</sup>	33.2	0.64
HP2	hot pressing at 1800°C, 80 MPa <sup>43</sup>	40.7	0.9

Table II. Hardness, Density, and Impurity Information on the Collected Samples

Sample Code	$H_v$ (1 kg) (GPa)	Density (g/cm <sup>3</sup> )	Impurity Levels
VPS2	11.0	5.88	XXX Al, X Ca, X Cr, X Cu, X Ni
VPS1	11.0	6.04	X Al
SHS	11.0	5.96	XX Al, X Fe, X Mn
HIP1	10.2	5.76	XX Al, X Cr, X Fe, X Zn
HIP2	9.2	6.23	XXX Al, X Cu, X Fe
HP1	9.2	5.96	XX Al
EHIP	9.5	6.24	X Al
HP2	8.3	6.21	X Al

note: X = 0.1-1wt%, XX = 0.5-5wt%, XXX = 1-10wt%

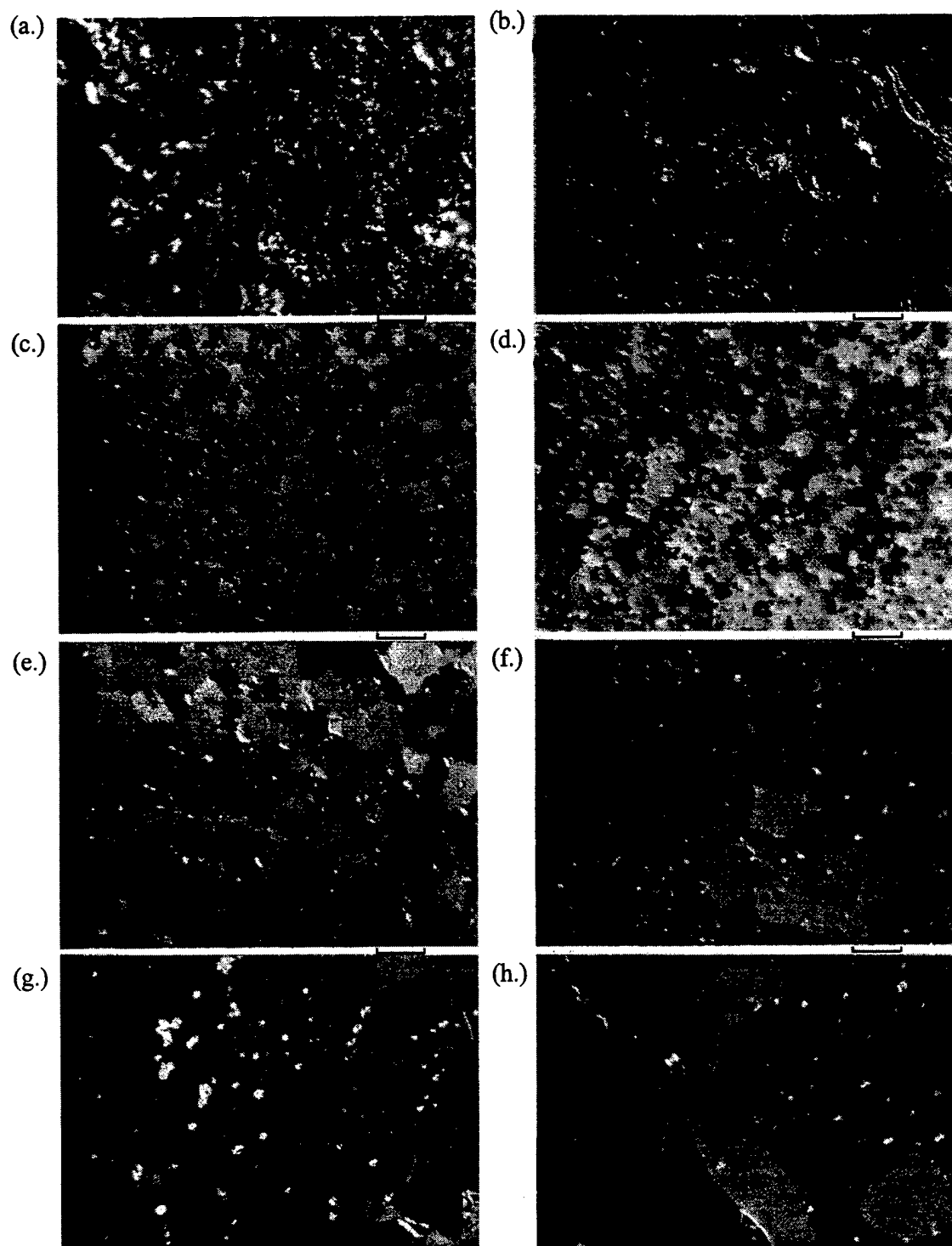


Figure 1. Optical micrographs of  $\text{MoSi}_2$  using cross polarized light of the following samples:(a.) VPS2 (b.) VPS1, (c.) SHS, (d.) HIP1, (e.) HIP2, (f.) HP1, (g.) eHIP, (h.) HP2. (Note: All micron markers are 10 microns in length)

### Purity

Spectrographic analysis of impurities has been conducted on the collected samples. The key impurities, other than oxygen, are identified in Table II. Aluminum is a typical impurity in  $\text{MoSi}_2$ , substituting for the Si in the C11b crystal structure,<sup>44</sup> while W or Cr are commonly observed substitutional elements for Mo.<sup>45</sup> The level of impurities may inhibit grain growth, due to the observation that all the higher impurity samples have a grain size of less than ten microns.

It is widely known that  $\text{MoSi}_2$  readily oxidizes in air to form a thin  $\text{SiO}_2$  scale. In the case of fine powders, significant oxygen pick-up occurs during particle size reduction and powder handling. For instance, as-reacted powder fragments typically contain 800 - 1000 ppm of oxygen. Upon milling, the <44 micron fraction shows oxygen levels of 2500 - 3000 ppm and further particle size reduction to produce fines increases the oxygen level to > 5000 ppm. Moreover, powder shelf-life is an important factor, because oxygen pick-up is likely to occur during long-term storage. Typically,  $\text{MoSi}_2$  fines or the <44 micron fraction are used for consolidating  $\text{MoSi}_2$ . A significant oxide presence is thus inevitable unless powder consolidation is conducted in highly controlled environments. The EHIP sample, described in Table I and Table II, was processed in an argon atmosphere glove-box and shows a significantly lower oxygen content than the other samples.

### Microstructural Variations

Figure 1 shows the microstructures of the various  $\text{MoSi}_2$  samples. The distinct differences in grain size and oxide content can readily be observed. The effect of processing methods on the consequent microstructure is discussed below.

In general, the hot pressed (HP) and hot isostatic pressed (HIP) samples show the largest grain sizes, while the reaction synthesis (SHS) and the plasma sprayed samples (VPS) show significantly finer grain sizes. Impurities, especially  $\text{SiO}_2$ , appear to play a role in retarding grain growth during processing. The impurity effect on grain growth is exemplified by comparing the EHIP sample with the HP1 samples. In spite of the lower HIP temperatures and finer starting particle sizes of the EHIP sample, the consolidated high purity material exhibited a significantly larger grain size. Furthermore, the HIP1 sample has a high level of oxide, leading to even finer grain size. The EHIP sample shows fine silica inclusions within the grains.

A silica phase is present in all of the samples, as observed by optical microscopy and oxygen analysis. The morphology of the silica depends on the sintering temperature, forming either a thin film of silica between grains at low temperatures or spherical precipitates dispersed trans- or intergranularly at high temperatures. At low stresses and temperature Sadananda *et al.*<sup>46</sup> report the relative contribution from grain boundary sliding to total creep rate can be significant. While at higher temperature, silica does not wet  $\text{MoSi}_2$ , according to Cotton *et al.*,<sup>47</sup> and creep is dominated by deformation of the grains.<sup>48</sup>

Rapid solidification of the molten  $\text{MoSi}_2$  particles during vacuum plasma spraying (VPS) produces a fine grained, chemically homogeneous microstructure.<sup>49</sup> In addition to forming polycrystalline regions of  $\text{MoSi}_2$  in both the C11b and C40 structures, a secondary phase of  $\text{Mo}_5\text{Si}_3$  has been detected by x-ray diffraction, confirming previous investigations on the processing of  $\text{MoSi}_2$  by VPS.<sup>9</sup> The distinct feature resulting from VPS processing is the fine-grained microstructure, with an apparently bimodal grain size distribution. Further, such materials contain silica inclusions that are significantly larger than the grain size.

Self-propagating high temperature synthesis (SHS) produces very high temperatures for a relatively short period of time (~20 seconds to 1000°C).<sup>6</sup> The high temperatures are a result of the heat of reaction associated with Mo and Si that result in a combustion wave propagating

through the sample. The short duration at high temperatures produces limited grain growth. The final processing step is to densify by hot pressing, and this permits the agglomeration of the silica.

Elemental hot isostatic pressing of MoSi<sub>2</sub> from low-oxide elemental powders produces a 99% dense product (EHIP sample). Hardwick *et al.*<sup>5</sup> observed that the higher silica level samples experienced less grain growth than the oxygen free samples. Silica is present in the EHIP sample both inter- and transgranularly. The results for the two other HIPped samples are a fine grain size HIP1 sample with an aggregate of silica, predominantly at the grain boundaries, and a larger grain size sample, HIP2, with silica decorating the grain boundaries and present within the grains.

The hot pressing of MoSi<sub>2</sub> powder requires higher temperatures than elemental powders to acquire full density. These higher temperatures will produce significantly greater grain growth, and may permit the agglomeration of the silica. The spheroidizing of the silica most likely takes place early in the process because a large fraction of the silica can be found within the grains.

#### Oxidation

Table III provides the results from the pesting oxidation study on the four samples examined. The silica and Mo<sub>5</sub>Si<sub>3</sub> levels, prior to oxidation of the samples, are also included in this table. Although no clear trend is observed, it appears that volume percent silica and Mo<sub>5</sub>Si<sub>3</sub> play a role in the oxidation behavior.

The growth of the oxide eventually forms a continuous oxide layer, as demonstrated in the XRD patterns in Figure 2, due to the disappearance of the MoSi<sub>2</sub> peaks as the oxide thickens. These four samples have been exposed to identical oxidation conditions prior to x-ray analysis. The HP1 sample produces the least amount of oxide product on its surface, which is demonstrated by the lack of MoO<sub>3</sub> peaks in the XRD pattern, and has the smallest weight change. The sample with the largest weight gain produces a continuous, although porous, oxide layer that eliminates any MoSi<sub>2</sub> peaks in the XRD pattern, so that only MoO<sub>3</sub> peaks remain. The other samples have a mixed pattern of MoSi<sub>2</sub> and MoO<sub>3</sub>. In addition, an amorphous SiO<sub>2</sub> background is observed in all of the samples except HP1. There is a significant fraction of SiO<sub>2</sub> in the oxide product due to the reaction.<sup>50</sup>

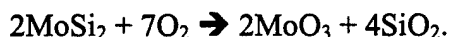


Table III Flowing Air Oxidation Test At 500°C.

Sample	Calculated Vol% SiO <sub>2</sub>	SEM Image Analysis Vol% SiO <sub>2</sub>	I (112) Mo <sub>5</sub> Si <sub>3</sub> / I (103) MoSi <sub>2</sub>	Oxidation Rate (mg/cm <sup>2</sup> )
HIP1	24.5%	10.9%	0.010	5.6
SHS	11.1%	6.5%	0.011	2.4
HP2	4.0%	3.7%	0.015	1.9
HP1	6.6%	N/A	0.007	0.07

Assuming that there are no other oxidation products, the volume percent silica is 64%, which is calculated from the molar fractions given in the above reaction. The volume fraction of silica is not clearly reflected in the XRD pattern because of its amorphous nature.

The oxidation rate appears to be influenced primarily by the purity levels, oxide content and  $\text{Mo}_5\text{Si}_3$  levels. The effect of the purity levels is consistent with Meschter's findings that an increase in impurities increases the rate of oxidation.<sup>51</sup> The two samples with a greater number of impurity elements, Table II, and a higher levels of  $\text{SiO}_2$  (HIP1 and SHS) appear to have a higher rate of oxidation. The level of silica is apparent from the micrographs in Figure 1, and silica can be present either inter- or transgranularly, as observed by the cross-polarized grain contrast of these optical images. The difference in the HP1 and HP2 samples, with similar impurities and silica content, is the level of  $\text{Mo}_5\text{Si}_3$ . The HP2 sample has more  $\text{Mo}_5\text{Si}_3$  and increased oxidation. Other studies have reported that the oxidation resistance of  $\text{Mo}_5\text{Si}_3$  is much less than that for  $\text{MoSi}_2$ .<sup>52</sup> HP1 sample has the lowest  $\text{Mo}_5\text{Si}_3$  content and a low level of silica among the four samples evaluated and clearly superior oxidation behavior.

This trend associated with the secondary phases may be attributed to the role of oxide nucleation at the surface. The surface morphology changes by having the oxide and/or  $\text{Mo}_5\text{Si}_3$  particles within the  $\text{MoSi}_2$  matrix. These oxide and/or  $\text{Mo}_5\text{Si}_3$  particles may inhibit the formation

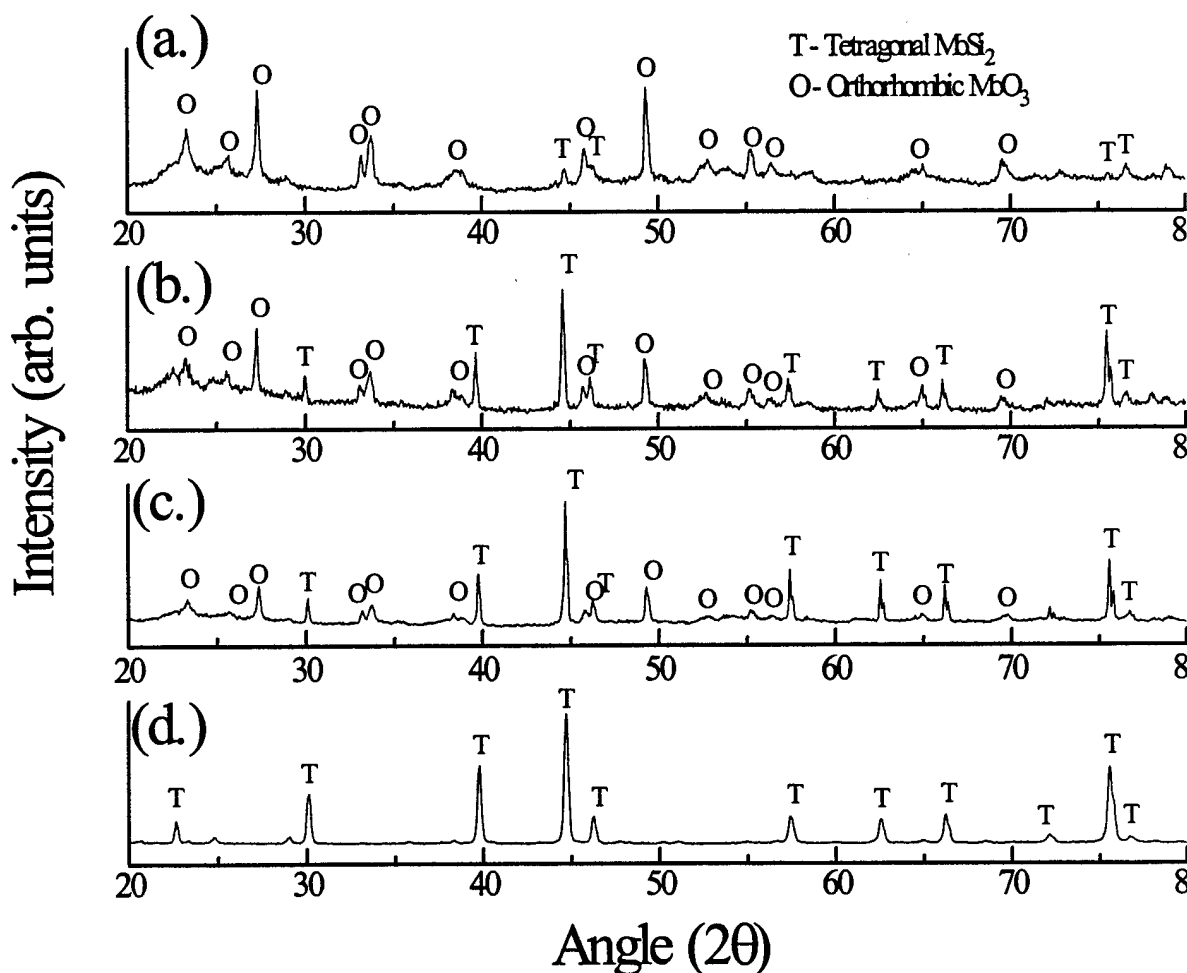


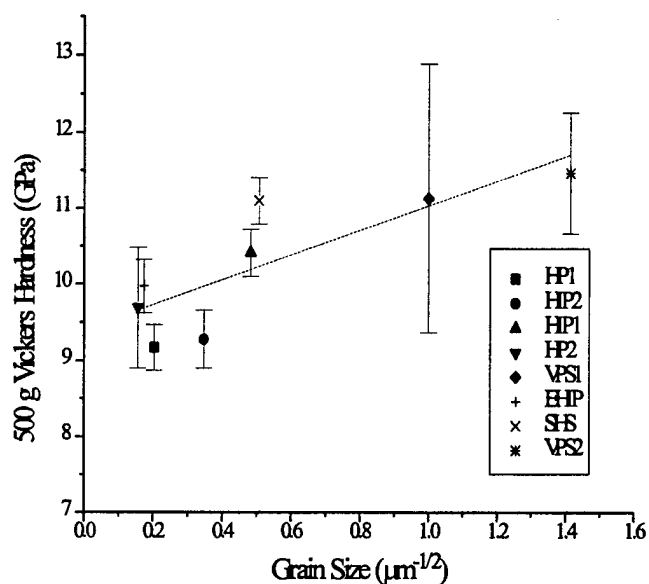
Figure 2. X-ray diffraction patterns of the samples' oxidation surfaces: (a.) HIP1, (b.) SHS, (c.) HP2, (d.) HP1.

of a thin, continuous oxide. The lateral growth of silica or silicates is required to produce a continuous oxide barrier, which limits further low temperature oxidation in  $\text{MoSi}_2$ .<sup>53</sup> The lowest oxidation rate, for the HP2 sample, may be primarily attributed to a low level of  $\text{Mo}_5\text{Si}_3$  and secondarily to a lower silica level.

### Indentation response of $\text{MoSi}_2$

#### Hardness

There is a 20% variation in hardness from the largest to the finest grain size samples; Table II. Fine grained samples show a higher hardness, which closely approximates a Hall-Petch type relationship, as illustrated in Figure 3. Some of the deviation from linearity is associated with the volume fraction of silica. For example, for the two samples with equivalent grain sizes,



#### HIP1 and

Figure 3. Hall-Petch type relationship of hardness, applying a linear fit to the measured values.

SHS, the hardness values are nearly equivalent when the silica volume fraction is accounted for by a rule of mixtures, with the silica hardness taken as 4.9 GPa. It is expected that the nonlinearity would be even less, if the purity levels, given in Table II, were less variant.

Table IV. Vickers, Nano, and Knoop Indentation Measurements

Sample	Vickers H <sup>*</sup> (GPa)	Nano H (GPa)	Knoop H <sup>**</sup> (GPa)
VPS1	11.2	16.5±4.4	10.5
VPS2		18.0±3.5	10.6
SHS	11.1	15.3±1.3	10.8
HIP1	10.4	15.2±1.8	9.9
HIP2	9.3	16.8±1.9	9.0
HP1	9.3	N/A	9.2
EHIP	9.5	16.2±1.7	9.7
HP2	9.5	17.5±2.0	9.0

• 9.8 N load, \*\* 4.4 N load

The hardness values for Vickers and Knoop indentations are listed in Table II. As expected, the two methods produce equivalent Vickers and Knoop values and the difference from the largest to smallest hardness values for these samples is 20%. The sampling area for the applied loads incorporates porosity and silica into the measurement. The large grain size and low silica content samples, HP2 and EHIP, have the lowest hardness values, as given in Table IV. The fine grain size samples with or without a substantial amount of silica have the largest hardness values. Surprisingly, one of the lowest hardness values is the HIP2 sample, which has neither the lowest silica content nor the largest grain size. This can be attributed to a significant level of the C40 phase present in this sample.

The nanoindentation hardness values are shown in Table IV. By accounting for the variation in the measured values, the results can be considered equivalent. The larger standard deviations associated with the nanoindentation of vacuum plasma sprayed samples, VPS1 and VPS2, compared to the standard deviations of the other samples are attributed to variations in microstructure on a nanoscale. Any differences associated with purity levels in these samples were not observed.

#### H/E Values

The hardness-to-elastic modulus ratio, H/E, described by indentation recovery for both nano- and micro-, are given in Table V. The H/E values are equivalent values on the nanoscale, indicating that the intrinsic response to the indentation is very similar for all samples irrespective of purity levels, but on a larger scale, measured by Knoop indentation, a variation in recovery is

Table V Indentation elastic/plastic response.

Sample	Nano H/E	Knoop H/E	Knoop (E/H) <sup>0.5</sup>	Knoop (E/H) <sup>0.5</sup> Normalized
VPS1	0.0425	0.034	5.42	1.14
VPS2	0.0390	0.036	5.27	1.11
SHS	0.0348	0.032	5.59	1.17
HIP1	0.0366	0.032	5.59	1.17
HIP2	0.0357	0.033	5.50	1.15
HP1	N/A	0.044	4.77	1.00
EHIP	0.0340	0.044	4.77	1.00
HP2	0.0359	0.032	5.59	1.17

seen. This variation can be attributed to permanent deformation consisting of plastic response and microcracking. The H/E value measured by Knoop indentation ranges from 0.1 to zero, with many ceramics and metals having a value near of 0.05. Typically, the hardness and modulus values are directly proportional, but the variation of their quotient describes their elastic/brittle and rigid/plastic responses. Materials that have a large H/E value are expected to be more elastic and brittle, for example soda-lime glass. In contrast, material with a low H/E value is more plastic and rigid, for example ZnO.<sup>54</sup> The lower degree of recovery in these samples is a product of microcracking and/or plastic deformation. The large grain size samples, EHIP and HP1, have a higher H/E value, indicating a higher degree of recovery. The six remaining samples have a lower recovery.

Similar to the nanoindentation hardness values, the H/E nanoindentation values are equivalent for all of the samples within a single standard deviation. Therefore, for the samples examined, purity has not been observed to affect the level of recovery. The changes in recovery observed by Knoop indentation are the result of microstructural changes.

### Indentation Cracking and Fracture Toughness

Indentation fracture toughness techniques has been used extensively to characterize the fracture toughness of MoSi<sub>2</sub>, as well as other brittle materials. Table VI provides the results reported in the literature for MoSi<sub>2</sub> and various MoSi<sub>2</sub>-based composites. Table VII provides the indentation fracture toughness values for the present set of samples obtained under different indentation loads. A wide variation in the results is observed ranging from a high of 7.9 MPam<sup>1/2</sup> (SHS at 1 kg) to 2.9 MPam<sup>1/2</sup> (HP1 at 10 kg). Additionally, the observation of higher value at low loads is contradictory to the observations made by Wade *et al.*<sup>4</sup> Although at higher loads, the toughness values are consistent with our work. Dependence of measured value on the applied load is observed, consistent with earlier results of Wade *et al.* The Anstis fracture toughness value is the largest for SHS, having a value of 7.9 MPam<sup>1/2</sup>, while the fracture toughness calculated by the radial crack length is 3.6 MPam<sup>1/2</sup>, as shown in Table VII and Table VIII. The other values measured by the two methods differ by up to a factor of two, but are consistent, having the HIP1 value being large and the HP2 value being small.

Table VI Indentation fracture toughness values for MoSi<sub>2</sub> and its composites.

Investigator	MoSi <sub>2</sub> K <sub>1c</sub>	Investigator	Compositing Addition	Composite K <sub>1c</sub>
Petrovic and Honnell <sup>8</sup>	2.58	Petrovic and Honnell <sup>8</sup>	30 v/o PSZ	6.56
Tiwari, Herman, and Sampath <sup>9</sup>	4.7, 5.9	Tiwari, Herman, and Sampath <sup>9</sup>	TiB <sub>2</sub> , SiC	6.1, 7.5
Bhattacharya and Petrovic <sup>10</sup>	2.85	Jeng, Wolfenstine, and Lavernia <sup>14</sup>	SiC	4.39
Bhaduri and Radhakrishnan <sup>11</sup>	2.88	Casto, Smith, Rollet, and Stanek <sup>12</sup>	20 v/o Ta	6.4
Casto, Smith, Rollet, and Stanek <sup>12</sup>	3.6, 5.7	Jayashankar, Riddle, and Kaufman <sup>63</sup>	20 v/o SiC	4.5
Wade and Petrovic <sup>13</sup>	3.0	Petrovic, Bhattacharya, Honnell, Mitchell, Wade, and McClellan <sup>29</sup>	20 v/o ZrO <sub>2</sub>	7.8

This wide scatter in the measured indentation fracture toughness values through the Anstis equation can be related to the nature of indentation cracking. As can be seen in Figure 4, a significant level of secondary cracking is observed in most of the samples, and only few of the

Table VII Grain size and Anstis fracture toughness at different loads of MoSi<sub>2</sub>.

Sample	Processing Method	Grain Size (micron)	K <sub>1c</sub> 1 kg (MPam <sup>1/2</sup> )	K <sub>1c</sub> 3 kg (MPam <sup>1/2</sup> )	K <sub>1c</sub> 10 kg (MPam <sup>1/2</sup> )
VPS1	vacuum plasma spraying	2.1	-	5.2	3.3
SHS	combustion synthesis	3.9	7.9	3.7	3.1
HIP1	hot isostatic pressing	4.3	5.5	-	-
HIP2	hot isostatic pressing	8.3	4.3	-	-
HP1	hot pressing	24.2	4.2	3.8	2.9
EHIP	hot isostatic pressing of elemental powders	21.3	5.7	3.8	3.9
HP2	hot pressing	40.7	-	3.1	-

samples satisfy the requisite radial-median cracking for measuring crack length. This study reveals that the traditional Anstis crack length measurement method needs to be used with caution to generate the fracture toughness values.

Table VIII shows the results of the total crack length (from all measurable cracks surrounding the indent). Significant differences in the total crack length are observed among the various samples, indicating a strong microstructural effect. This is addressed in greater detail in the subsequent section. Table VIII also reveals the length of the single longest indent crack, independent of the indent corners, for each sample. This was utilized to evaluate the response of the microstructure to crack propagation in these materials. The  $K_{Ic}$  was calculated for their single longest crack using the Anstis equation. The adjusted  $K_{Ic}$  values given in Table VIII account for the  $E/H^{1/2}$  term in the Anstis equation rather than using the bulk elastic modulus, in order to account for the H/E response. This adjustment changes the fracture toughness value by up to 17%.

Table VIII Crack length measurements, acoustic emission response, and fracture toughness values

Sample Code	Cumulative Length	Radial Distance	Maximum Amplitude (dB) ***	Total Number of Events	Radial $K_{Ic}$ *	Adjusted Radial $K_{Ic}$ (3 kg) **
VPS1	n/a	n/a	62.6	318±24	2.67	3.04
VPS2	n/a	n/a	n/a	n/a	4.08	4.51
SHS	71±21	73±9	59.8	166±16	3.58	4.20
HIP1	104±37	40±5	58.4	278±18	4.70	5.51
HIP2	308±47	64±4	n/a	n/a	2.34	2.70
HP1	286±54	54±7	65.8	129±32	2.50	2.50
HP2	325±81	58±12	66.3	42±7	2.23	2.23
EHIP	271±26	56±15	n/a	n/a	1.73	2.03

\* Single longest radial crack used to calculate Anstis fracture toughness.

\*\* Applying E/H value from Table III with Anstis fracture toughness.

\*\*\* The amplitudes are an average of ten indentations.

#### Acoustic Emission

The cracking morphology described thus far pertains to observable surface cracks created during indentation. However, these do not reveal the presence of sub-surface cracks. In an effort to complement the crack length measurement analysis, acoustic emission was used to quantify the cracking response. Table VIII provides the acoustic emission results for some of the samples. The total number of cracking events and the maximum amplitude are included. The acoustic emission results are consistent with the total crack length measurement for these samples, i.e. large numbers of small events are observed when associated with short crack lengths, while long cracks lead to fewer, highly energetic acoustic emission events. With regard to the highest decibel acoustic activity, cracking was attributed to the sample with the smallest amount of grain boundary area, i.e., largest grain size sample (HP2), as shown in Table VIII. On the contrary, the sample with a small grain size and the largest fraction of silica has the lowest peak acoustic activity. The number of acoustic events indicates the quantity of cracking events. The correlation of acoustic events to the sample's grain size indicates the largest number of events for the finest grain size sample, VPS1, and conversely, the least number of events for the largest grain size sample, HP2. In addition, the average interfacial area between the silica and the  $MoSi_2$  is directly proportional to the number of acoustic events, as given in Table VIII. The interfacial surface areas between silica and the matrix phase of the samples are determined from the microstructures in Figure 1. The specific surface area calculations assume spherical particles of equal size, justified by the large differences in silica sizes between samples.

#### Measurement and Interpretation of Cracking/Toughness

The crack paths surrounding the 3 kg Vickers indentations of the samples examined in this study are given in Figure 4. These crack traces are indicative of the differences in cracking behavior. In general, the fine grained samples displayed cracks emanating predominantly from the four corners of the Vickers indent, while coarse grained samples exhibit secondary cracking.

Indentation methods have been used to evaluate unreinforced  $\text{MoSi}_2$  samples for their fracture toughness. Although this technique is prone to considerable variability, the ease of measurement makes it possible to evaluate a large number of samples produced under different conditions. As noted in Table VI, indentation fracture toughness measurements reported in the literature differ by up to a factor of 2.3 for unreinforced  $\text{MoSi}_2$ <sup>55-60</sup> and by a factor of 1.8 for its composites.<sup>10,61-64</sup> Fracture toughness measurements from this study are summarized in Table VII and show that the indentation load is a factor causing variability in the reported values.

Two limitations can help to explain the variability in reported literature results for the fracture toughness of bulk  $\text{MoSi}_2$  as obtained by the Anstis fracture toughness equation.<sup>65</sup> First, the different values of  $K_{Ic}$  as a function of load indicates that  $P/c^{3/2}$  is not constant, as shown in Table V that includes the  $K_{Ic}$  values for one, three, and ten kilogram loads. For example, the SHS sample has a value of  $7.9 \text{ MPam}^{1/2}$  at 1 kg and  $3.1 \text{ MPam}^{1/2}$  at 10 kg. The fracture toughness value of  $7.9 \text{ MPam}^{1/2}$  for SHS at a 1 kg load is misleading due to small crack lengths at this low load. Second, the stress associated with the anisotropic coefficient of thermal expansion will modify the Boussinesq stress field<sup>66</sup> for the large grain size samples. Further, the rapid solidification of the most fine grained samples will add residual stresses to the sample. The changes in the stress field result in different crack patterns.

#### Effect of Silica on Cracking Behavior

The increase of silica in the system, particularly if a thin film exists at the grain boundaries, has the possibility of weakening the bonding. A highly energetic acoustic signal has been observed with other systems having silica<sup>67</sup> and  $\text{MnS}$ <sup>68</sup> inclusions. The interface between silica and  $\text{MoSi}_2$  is a site for flaw nucleation and a means of deflecting propagating cracks, as shown in the microstructures in Figure 5 b and 6d. Cracking in all the examined samples appears to be influenced by the silica- $\text{MoSi}_2$  interface, even with a large grain size sample, because the silica is dispersed throughout the microstructure both within the grains and at the grain boundaries. The anomalously large amplitude of VPS1 can be attributed to its 4mm thickness compared to the other samples that have a 5 mm thickness.

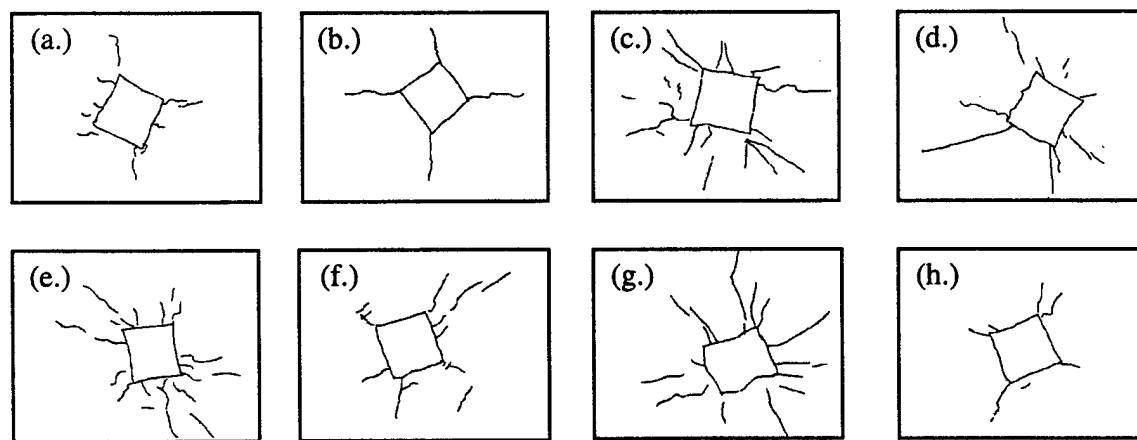


Figure 4. Crack patterns produced by Vickers indentation at 3 kg load: (a.) HIP1, (b.) SHS, (c.) EHIP, (d.) HIP2, (e.) HP1, (f.) VPS2, (g.) HP2, (h.) VPS1.

The two samples, SHS and HIP1, that have similar crack traces are presented in Figure 4 to illustrate the differences in their cracking behavior. These two samples have nearly the same grain size, but the HIP1 sample has more than a 150% increase in total acoustic emission (AE) events. The crack path is much less tortuous in SHS than in HIP1, Figure 5a and 6c. In addition,

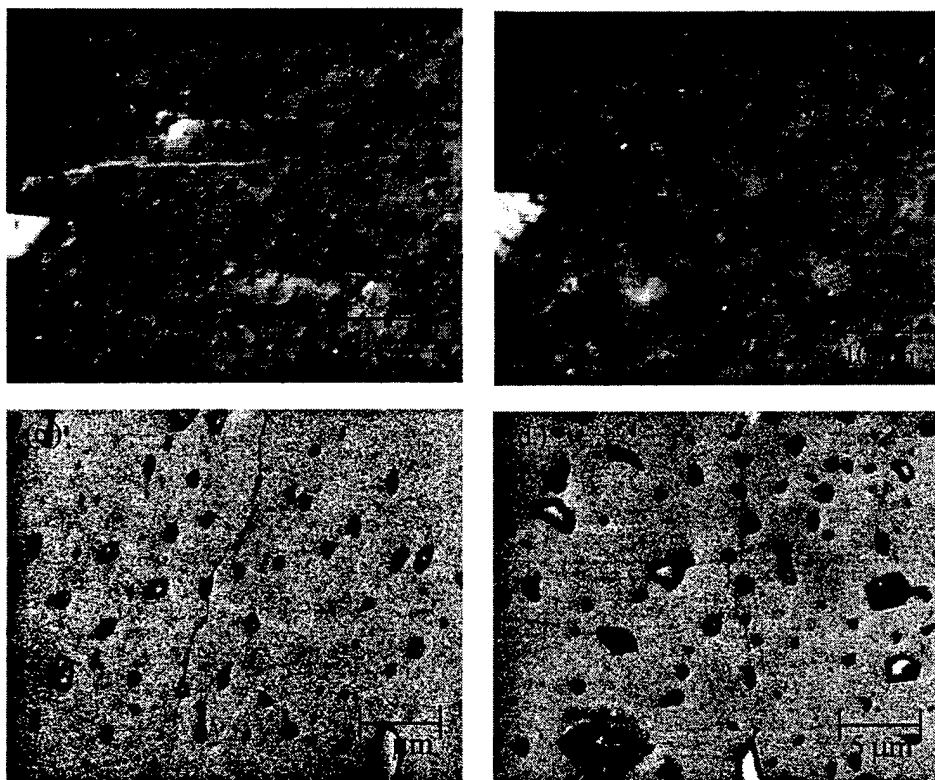


Figure 5. Transgranular cracking observed in SHS (a,c) and intergranular cracking in HIP1 (b,d).

there is less interaction with the silica in the SHS sample, following a single transgranular crack path. The differences in cracking are attributed to the level of silica and its distribution. The low processing temperature for the HIP1 sample minimizes spheroidization of silica at grain boundaries. The HIP1 sample cracks almost entirely intergranularly, due to the 14 vol% silica that exists between the  $\text{MoSi}_2$  grains, while the SHS sample cracks inter- and transgranularly due to its lower silica content. The intergranular fracture of HIP1 leads to the most tortuous crack path and shortest propagating cracks, hence, suggesting greatest fracture toughness.

#### Effect of Grain Size on Cracking Behavior

An analogous cracking and deformation mechanism to improve fracture toughness, similar to that described in the NiAl system,<sup>69,70</sup> may be applicable to  $\text{MoSi}_2$ . Table II, Table V, Table VII, Table VIII provide information on the effect of grain size on mechanical properties. Clearly, finer grain sizes, such as those associated with VPS formed materials, yield greater hardness and improved Anstis fracture toughness.

The HIP1 sample has the largest  $K_{Ic}$ , Table VII, and fractures exclusively intergranularly. The intergranular fracture is the result of two microstructural features: (1) increased availability of grain boundaries in the crack's path with a fine grain size, and (2) weakening of boundaries by

a siliceous grain boundary phase, as mentioned previously. In addition, the silica can cause Zener drag that minimizes grain growth during processing. An example of repressing grain growth in  $\text{MoSi}_2$  is the HIP1 sample that contains 14 vol% silica, which is compared to the EHIP sample that has a processing temperature within  $50^\circ\text{C}$  and has a factor of seven larger grain size, Table I.

The cracking behavior of the two VPS samples are very similar to one another. The presence of a few large grains in the VPS samples produce transgranular cracking. Although the oxide content is significant in the VPS1 and VPS2 samples, the silica is observed as large inclusions rather than as fine particles, in contrast to the SHS sample.

The maximum amplitudes for the samples are noted in Table VIII and indicate a high energy event. A large crack, especially coupled with fracturing through a grain, produces a large acoustic signal. The amplitude values are in decibals with each unit indicating an order of magnitude change in value. The source of the high amplitude events could be either due to large cracks, stronger bonding, or simultaneous cracking. The HP1 and HP2 samples have the longest cracks as well as the largest maximum AE amplitudes, while samples with the more tortuous crack path have lower maximum AE amplitudes. Total crack length measurements surrounding an indent are confirmed by optical microscopy and are given in Table VIII. The largest grain size sample, HP1, has the greatest cumulative crack length measurement.

The fine grained size samples (SHS and HIP1) did not have large total cracks lengths, but the cracking path is tortuous and a large number of acoustic events were detected, Table VIII and Figure 5. There is little slip observed in these samples compared to the large grained samples, indicating a preference to microcracking as the mechanism for damage accumulation rather than a plastic response. The cracking of VPS1 and VPS2 samples produces a network of intergranular cracks near the corners of the indent.

### *Effect of alloying and compositing on the properties of $\text{MoSi}_2$*

#### Microstructural Features

The large grain size in the HP2 sample is due in part to the high processing temperature,  $1880^\circ\text{C}$ . Additionally, a bimodal particle size distribution of the starting powder allowed for considerable secondary recrystallization, as evidenced by the concave grain boundaries in Figure 6(a). The EHIP sample has a somewhat finer grain size due to its lower processing temperature, Figure 6(b). Both samples possess  $> 99\%$  density, due to similar processing methodology. However, the EHIP sample contains a lower level of silica due to an inert atmosphere processing environment.

The 13.3Al and 33.3Al samples have a grain size similar to that for the EHIP sample. However, the Al-poor sample,  $\text{Mo}(\text{Si}_{0.8}\text{Al}_{0.2})_2$ , results in a change in crystal structure from tetragonal C11b to hexagonal C40. Additionally, in the Al-rich sample, 33.3Al, the presence of orthorhombic C54 has been tentatively identified. The C54 has been previously identified by Stergiou *et al.*<sup>71</sup> in an alloy of composition  $\text{Mo}(\text{Si}_{0.66}\text{Al}_{0.33})_2$ . Figure 6(c), 13.3Al, indicates that some grains display no precipitates while others show precipitates dispersed throughout the grain. The precipitates are likely C40 in the C11b grains, due to the higher level of Al in the precipitate in comparison with the surrounding matrix, as determined by energy dispersive spectroscopy. The microstructure of 33.3Al shows no precipitates that are present in 13.3Al, as shown in Figure 6 (c) and (d).

The sample with the Re addition was produced by co-melting of  $\text{MoSi}_2$  and  $\text{ReSi}_2$  powders. Further information about the processing can be found in the literature.<sup>37</sup> The Re modified  $\text{MoSi}_2$  sample has a density of  $6.48 \text{ g/cm}^3$ , measured by the Archimedian water immersion technique. The porosity level is 5.4%, obtained by comparing the measured density to

Table IX Processing Methods and Microstructural Features

Sample	Composition	Processing	Grain Size( $\mu\text{m}$ )	References
HP2	MoSi <sub>2</sub>	Hot pressing at 1880°C	41	72
EHIP	MoSi <sub>2</sub>	Elemental powders, hot isostatic pressing at 1400°C	33	5
13.3Al	Mo(Si <sub>0.8</sub> Al <sub>0.2</sub> ) <sub>2</sub>	Arc cast, hot isostatic pressed at 1500°C, homogenized at 1400°C/ 48 hrs.	10-40	73
33.3Al	Mo(Si <sub>0.5</sub> Al <sub>0.5</sub> ) <sub>2</sub>	Same as 13.3Al	10-40	73
5.6Re-C	(Mo <sub>0.83</sub> Re <sub>0.17</sub> )Si <sub>2</sub>	Arc cast, hot isostatic pressed at 1850°C/ 8 hrs.	10-75	74
MA MoSi <sub>2</sub> / 20 SiC	MoSi <sub>2</sub> - 20 vol% SiC	in-situ formed MoSi <sub>2</sub> /SiC, 1650°C/ 1 hr	2-7 (MoSi <sub>2</sub> ) 1-10 (SiC)	75

the theoretical density. The theoretical density is calculated from the XRD lattice spacings. The porosity in this sample is the result of large sized pores; an example of the pore size is shown in Figure 6(e). The MoSi<sub>2</sub>-SiC composite is fabricated by an *in situ* displacement reaction using starting powders of Mo, Si, and C. The reaction takes place in a porous compact to permit the CO and CO<sub>2</sub> gases to escape and to prevent grain growth. After completion of the reaction, the compact is fully consolidated by vacuum hot pressing. The limited grain growth is attributed to the presence of SiC particles, as shown in Figure 6(f).

### Mechanical Properties

The hardness and cracking responses resulting from 30 N Vickers indentations are listed in Table X. The hardness values range from 6.6 to 12.6 GPa and the Anstis fracture toughness values range from 1.9 to 4.0 MPa<sup>1/2</sup>. The cracking behavior differs substantially among the samples, as shown in Figure 7. Possible toughening mechanisms associated with the observed fracture behavior are discussed below.

The only sample that conforms to the ideal radial/median cracking behavior, as set forth by Evans *et al.*, is the MoSi<sub>2</sub>-SiC composite.<sup>76</sup> Various researchers<sup>8-13</sup> have employed the indentation technique to calculate fracture toughness values for unreinforced MoSi<sub>2</sub>, implementing the Anstis relation,<sup>65</sup> even though the requirements for ideal radial/median crack systems are not strictly followed due to the observed secondary cracks. The following analysis of cracking behavior and toughening mechanisms in MoSi<sub>2</sub> is based on three test methods: (1) Anstis relation, (2) single longest crack, irrespective of whether the crack meets with the corners of the indent, and (3) total crack length.

Samples HP2 and EHIP predominantly fracture transgranularly with minimal interactions between the crack and the silica. This mode of fracture is due to the small number and size of the SiO<sub>2</sub> particles. In addition, the dominance of secondary cracking over radial cracking from the indent corners, as shown in Figure 7(a) and 7(b), is attributed to the samples large grain sizes that create substantial residual stresses due to the anisotropic CTE values.

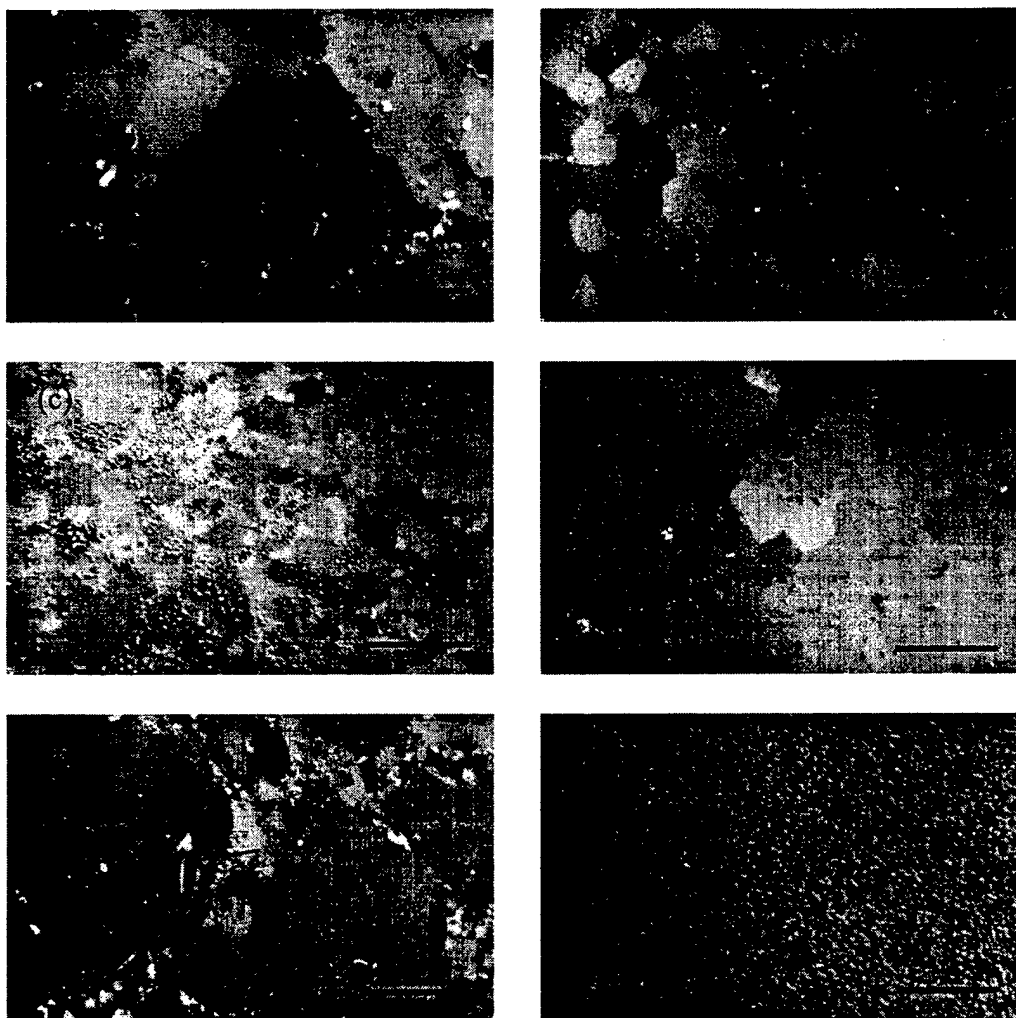


Figure 6. Optical micrographs using cross-polarized light with nomarski: (a) HP2, (b) EHIP, (c) 13.3Al, (d) 33.3Al, (e) 5.6Re, (f) MA MoSi<sub>2</sub>/ 20 SiC (Markers are 50 microns)

The samples containing 13.3 and 33.3 at% Al additions exhibit different cracking responses when subjected to a 30N Vickers indentation. These differences are consistent with their microstructural differences. The 13.3Al sample has an improved longest crack fracture toughness over the 33.3Al sample (Table X). Further indication that the 13.3Al sample has improved fracture toughness is the 33% reduction in total crack length measurement. The source of the differences in fracture behavior must lie elsewhere, because 13.3Al and 33.3Al have similar grain sizes, as shown in

Table IX. Figure 7(c), sample 13.3Al, illustrates that cracks propagating through grains containing precipitates follow a tortuous crack path by being deflected by the precipitates, while cracks traveling through the precipitate-free grains propagate in a straight path. The cracking shown in Figure 7(d), 33.3Al, follows straight crack paths due to absence of precipitates. The fracture toughness can be further improved by having a large aspect ratio to the secondary phase, as noted by Faber *et al.*<sup>77</sup> In addition, the combination of precipitates and crystal structure changes results in a 30% increase in hardness for the 13.3Al sample.

Table X Hardness Values and 30 N Vickers Indentation Crack Length Analyses

Sample	H <sub>v</sub> (500g) (GPa)	Longest Crack (μm)	Anstis K <sub>1c</sub> (MPam <sup>1/2</sup> )	Longest Crack K <sub>1c</sub> (MPam <sup>1/2</sup> )	Total Crack Length/Indent (μm)
HP2	9.5	159	3.2	2.2	1080
EHIP	9.5	132	3.3	2.0	1020
13.3Al	8.7	112	4.0	3.3	1090
33.3Al	6.6	174	1.9	1.5	1635
5.6Re	9.4	196	2.0	1.2	1320
MA MoSi <sub>2</sub> / 20 SiC	12.6	92	4.1	3.6	365

Re substitutes for Mo on the Mo sub-lattice of MoSi<sub>2</sub> and alters the lattice spacings without changing the crystal structure. The 5.6 at% Re addition produces the largest total crack length and smallest long crack fracture toughness value, as shown in Table X. The low fracture toughness is attributed to two factors: residual stresses and porosity. First, due to the anisotropic CTE values, the sample's large grain size yields large residual stresses that in turn enhances cracking.<sup>78</sup> Second, the 5.4% porosity enhances crack propagation. The lack of secondary particles or precipitates accentuates the low fracture resistance of the sample. The conservative measurement of the fracture toughness values is exemplified by the chevron-notched fracture toughness values of 2.7 and 3.8 MPam<sup>1/2</sup> for tests reported by Davidson *et al.*,<sup>37</sup> compared to the 2.0 and 1.2 MPam<sup>1/2</sup> values, measured by the Anstis relation and longest crack methods, respectively. The hardness values reported in this work are lower than that reported by Davidson due to the load used, 500 grams versus 25 grams, respectively. The change in values can be attributed to cracking and interacting with pores.

The silica-free MoSi<sub>2</sub>/SiC composite has an equivalent fracture toughness of 13.3Al. This composite has the advantage of reduced stresses resulting from the fine grain size and small SiC particles as well as a homogenous distribution of the SiC particles which can aid in deflecting propagating cracks. Further improvements in fracture toughness for MoSi<sub>2</sub>/SiC composites can be due to the presence of silica, as reported by Jayashankar *et al.*<sup>63</sup> The significant increase in hardness to 12.6 GPa is attributed to the fine grain size and the compositing effect of the SiC.

### SUMMARY AND CONCLUSION

The MoSi<sub>2</sub> samples examined in this study demonstrate that the variability in the microstructure and properties of bulk MoSi<sub>2</sub> depend on the processing method. More specifically, the grain sizes and silica levels vary from 1 to 40 microns and 1.7 to 14 vol%, respectively. With regard to low temperature oxidation, the pest oxidation rate depends on impurities and phase distribution.

The hardness, elastic/plastic response, and fracture toughness also vary significantly. The hardness variation can be attributed mostly to grain size and the elastic/plastic response modifies the fracture toughness by up to 14%. The fracture toughness, i.e., resistance to crack propagation, was evaluated by crack lengths and paths surrounding the indentations and *in situ* acoustic emission. Samples with the lowest total crack length and shortest propagating crack length indicate a propensity for larger fracture toughness values. The fracture toughness

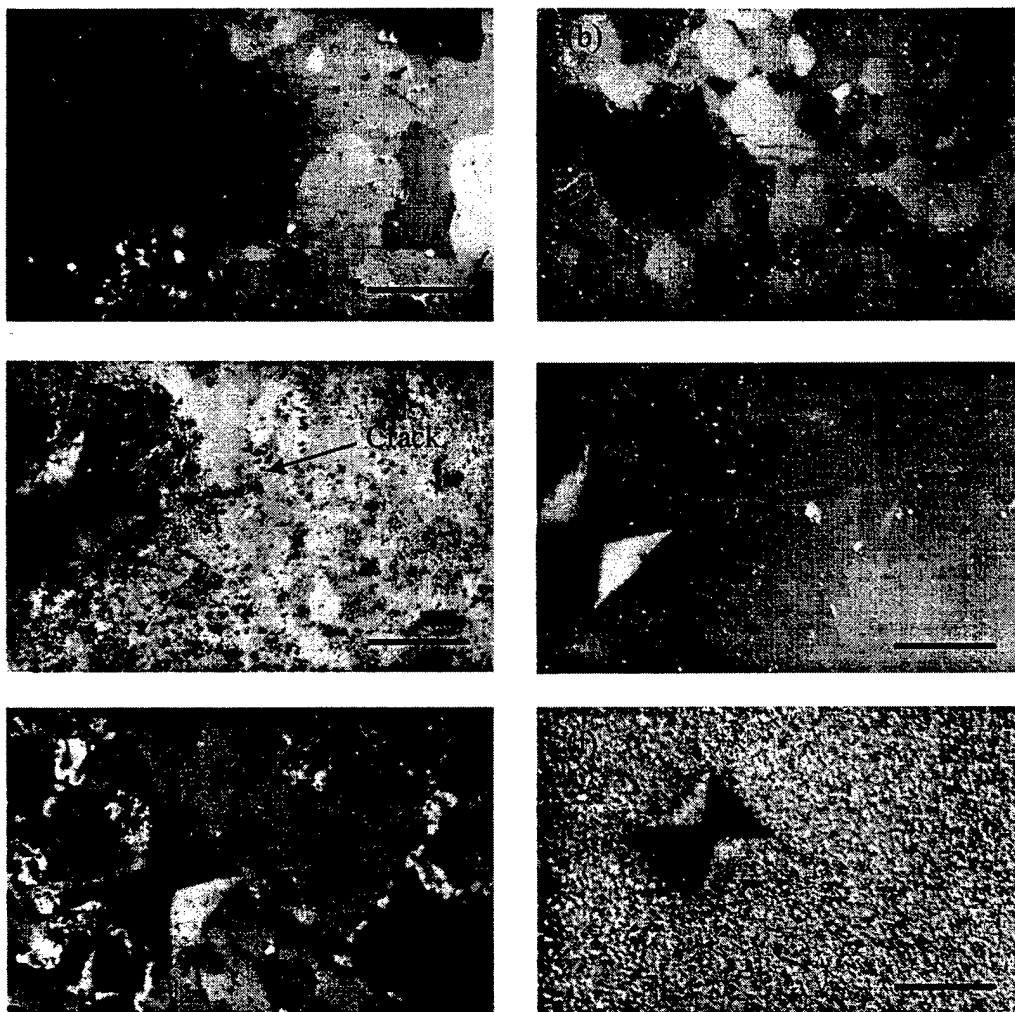


Figure 7. Crack paths from a 30 N Vickers indentation: (a) HP2, (b) EHIP, (c) 13.3Al, (d) 33.3Al, (e) 5.6Re, (f) MA MoSi<sub>2</sub>/ 20 SiC (Markers are 50 microns).

estimates, accounting for variation in H/E, range from 2.0 to 5.5 MPam<sup>1/2</sup> for these samples. As observed in optical and SEM micrographs, the silica provides flaw sites to nucleate microcracks and crack deflection. A fine dispersion of silica combined with a fine grain size provides the greatest fracture toughness. The acoustic emission results are consistent with the observed crack paths. The tortuous crack path, making for a greater fracture toughness, produces more acoustic emission events. The large grain size samples with fewer weak boundaries produces fewer acoustic emission events that have a lower maximum amplitude.

The microstructure and cracking behavior of unreinforced MoSi<sub>2</sub> change with Al, Re, and SiC additions. The fracture toughness values for these samples are evaluated with indentation by measuring the crack lengths surrounding the indentation. The two-phase microstructure, which is present in the 13.3 at% Al sample, and the secondary phase particles, which are present in the composite, are useful in creating crack deflection and, hence, in improving fracture toughness. A microstructure including precipitates and compositing additions (e.g., SiC, Si<sub>3</sub>N<sub>4</sub>) could lead to a synergistic relationship that would further improve fracture toughness values and, potentially, high temperature properties.

1. D. M. Shah, D. Berczik, D. L. Anton, and R. Hecht, *Mat. Sci. and Eng.*, A155 (1992) 45-58.
2. E. Fitzer, Molybdandisilizid als Hochtemperatureswerkstoff, in F. Benesovsky (ed.), *Proc. 2nd Plansee Semin.*, Springer, Berlin (1955) 56-79.
3. A. K. Vasudevan and J. J. Petrovic, *Mat. Sci. and Eng.*, A155 (1992) 1-18.
4. R. K. Wade and J. J. Petrovic, *J. Am. Ceram. Soc.*, 75(6) (1992) 1682-84.
5. D. A. Hardwick, P. L. Martin, and R. J. Moores, *Scripta Metall. Mater.* 27(1992) 391.
6. S. C. Deevi, *J. Mat. Sci.*, 26 (1991) 3343-3353.
7. S. Sampath, R. Tiwari, and H. Herman, in *Proceedings of the TMS Symposium on Microstructural Design by Solidification Processes*, E. J. Lavernia and M. N. Gungor, Editors, p. 151, TMS, Warrendale, Pa (1992).
8. J. J. Petrovic and R. E. Honnell, *J. of Mat. Sci.*, 25 (1990) 4453-4456.
9. R. Tiwari, H. Herman, and S. Sampath, *Mat. Sci. and Eng.*, A155 (1992) 95-100.
10. A. K. Bhattacharya and J. J. Petrovic, *J. Am. Ceram. Soc.*, 74(10) (1991) 2700-2703.
11. S. B. Bhaduri and R. Radhakrishnan, *Advances in Powder Metallurgy & Particulate Materials—Vol. 9. Particulate Materials and Processes*, San Francisco, California USA, 21-26 June 1992, p. 369-379.
12. R. G. Castro, R. W. Smith, A. D. Rollett, and P. W. Stanek, *Scripta Metall.*, 26 (1992) 207-212.
13. R. K. Wade and J. J. Petrovic, *J. Am. Ceram. Soc.*, 75(11) (1992) 3160-62.
14. Y. L. Jeng, J. Wolfenstine, and E. J. Lavernia, *Scripta Metall.*, 28 (1993) 453-458.
15. Matthias, K., Ph.D Thesis, Universitat Karlsruhe, 1969.
16. D. A. Hardwick, P. L. Martin, and R. J. Moores, *Scripta Metall. Mater.* 27 (1992) 391.
17. R. M. Aikin, Jr., *Scripta Met.*, 26 (1992) 1025-1030.
18. K. Ito, T. Yano, H. Inui, and M. Yamaguchi, *Mat. Res. Soc. Symp. Proc.*, High Temperature Ordered Alloys VI, Eds. J. A. Horton, I. Baker, S. Hanada, R. D. Noebe, D. S. Schwartz, Vol. 364 (1995) 899-904.
19. J. D. Cotton, Y. S. Kim, and M. J. Kaufman, *Mat. Sci. and Eng.*, A144 (1991) 287-291.
20. A. Costa e Silva and M. J. Kaufman, *Met Trans A*, 25A (1) (1994) 5-15.
21. T. C. Chou and T. G. Nieh, *J. Mater. Res.*, 8(1) (1993) 214-226.
22. S. Maloy, A. H. Heuer, J. Lewandowski, and J. Petrovic, *J. Amer. Ceram. Soc.*, 74(10) (1991) 2704-2706.
23. F. W. Vahldiek, and S. A. Mersol, *J. Less-Comm. Met.*, 15 (1968) 165-176.
24. P. H. Boldt, J. D. Embury, and G. C. Weatherly, *Mat. Sci. and Eng.*, A155 (1992) 251-258.
25. K. Ito, T. Yano, H. Inui, and M. Yamaguchi, *Mat. Res. Soc. Symp. Proc.*, High Temperature Ordered Alloys VI, Eds. J. A. Horton, I. Baker, S. Hanada, R. D. Noebe, D. S. Schwartz, Vol. 364 (1995) 899-904.
26. M. Hebsur, *Intermetallic Matrix Composites III*, eds. J. A. Graves, R. R. Bowman, and J. J. Lewandowski, 350 (1994) 77-182.
27. J. J. Petrovic and R. E. Honnell, *J. of Mat. Sci. Lett.*, 9 (1990) 1083-1084.
28. R. M. Aikin, Jr., *Ceram. Eng. Sci. Proc.*, 12(9-10) (1991) 1643-1655.
29. J. J. Petrovic, A. K. Bhattacharya, R. E. Honnell, T. E. Mitchell, R. K. Wade, and K. J. McClellan, *Mat. Sci. and Eng.*, A155 (1992) 259-266.
30. R. Gibala, H. Chang, and C. M. Czarnik, *High Temperature Silicides and Refractory Alloys*, eds. C. L. Briant, J. J. Petrovic, B. P. Bewlay, A. K. Vasudevan, H. A. Lipsitt, 322 (1994) 175-184.
31. I. Baker and P. R. Munroe, *J. of Met.*, 40(2) (1988) 28-31.
32. R. Darolia, D. Lahrman, and R. Field, *Scripta Met.*, 26 (1992) 1007-1012.
33. M. Yamaguchi and Y. Umakoshi, *Prog. Met. Sci.*, 34 (1990) 22,118.
34. Y. Umakoshi, T. Hirano, T. Sakagami, and T. Yamane, *High Temperature Aluminides and Intermetallics*, edited by S. Whang, C. Liu, D. Pope, and J. Stiegler (TMS, Warrendale, PA, 1990) 111-129.
35. A. Stergiou and P. Tsakirooulos, *Mat. Res. Soc. Symp. Proc.*, High Temperature Ordered Alloys VI, Eds. J. A. Horton, I. Baker, S. Hanada, R. D. Noebe, D. S. Schwartz, Vol. 364 (1995) 911-916.
36. S. Chin, D. L. Anton, and A. F. Giamei, *Material Research Society Symp. Proc. High Temperature Structural Applications in High Temperature Silicides and Refractory Alloys*, eds. C. L. Briant, J. J. Petrovic, B. P. Bewlay, A. K. Vasudevan, H. A. Lipsitt, Vol. 322 (1994) 423-429.
37. D. L. Davidson and A. Bose, *High Temperature Silicides and Refractory Alloys*, eds. C. L. Briant, J. J. Petrovic, B. P. Bewlay, A. K. Vasudevan, H. A. Lipsitt, 322 (1994) 431-436.
38. W. C. Oliver and G. M. Pharr, *J. Mater. Res.*, 7(6) (1992) 1565-1570.
39. G. R. Anstis, P. Chantikul, B. R. Lawn, and D. B. Marshall, *J. Amer. Ceram. Soc.*, 64(9) (1981) 533-538.
40. R. G. Castro, R. W. Smith, A. D. Rollett, and P. W. Stanek, *Mat. Sci. Eng.*, A155, 101-8, 1992.
41. D. Alman, personal communication, Jan., 1995.
42. M. Hebsur, *Intermetallic Matrix Composites III*, MRS Proc. 350, 177-182, 1994.

43. R. Tiwari, H. Herman, S. Sampath, and B. Gedmundsson, *Mat. Sci. Eng.*, A144, 127 (1991).
44. A. Costa e Silva and M. J. Kaufman, *Scripta Met.*, 29, 1141-1145, 1993.
45. Y. Umakoshi, T. Hirano, T. Sakagami, and T. Yamane in *High Temperature Aluminides and Intermetallics*, edited by S. Whang, C. Liu, D. Pope, and J. Stiegler (TMS, Warrendale, PA, 1990), p 111-129.
46. K. Sadananda, H. Jones, J. Feng, J. J. Petrovic, and A. K. Vasudevan, *Ceram. Eng. Sci. Proc.*, 12 (9-10) (1991) 1671-1678.
47. J. D. Cotton, Y. S. Kim, and M. J. Kaufman, *Mat. Sci. and Eng.*, A144 (1991) 287-291.
48. K. Sadananda, C. R. Feng, H. Jones, and J. J. Petrovic, *Mat. Sci. and Eng.*, A155 (1992) 227-240.
49. S. Sampath and H. Herman, D. L. Houch (ed.), *Thermal Spray: Advances in Coating Technology*, American Society for Metals, Metals Park, OH, 1988, p. 1.
50. C. D. Wirkus and D. R. Wilder, *J. Am. Ceram. Soc.*, 49 (1966) 173-177.
51. P. J. Meschter, *Met. Trans. A*, 23A (1992) 1763-17.
52. C. G. McKamey, P. F. Tortorelli, J. H. DeVan, and C. A. Carmichael, *J. Mater. Res.*, 7(10) (1992) 2747-2755.
53. H. J. Grabke and G. H. Meier, *Oxid. of Met.*, 44(1/2) (1995) 147-176.
54. D. B. Marshall, T. Noma, and A. G. Evans, *J. Amer. Ceram. Soc.*, 65(10) (1982) C175-176.
55. J. J. Petrovic and R. E. Honnell, *J. of Mat. Sci.*, 25 (1990) 4453-4456.
56. R. Tiwari, H. Herman, and S. Sampath, *Mat. Sci. and Eng.*, A155 (1992) 95-100.
57. A. K. Bhattacharya and J. J. Petrovic, *J. Am. Ceram. Soc.*, 74(10) (1991) 2700-2703.
58. S. B. Bhaduri and R. Radhakrishnan, *Advances in Powder Metallurgy & Particulate Materials--Vol. 9. Particulate Materials and Processes*, San Francisco, California USA, 21-26 June 1992, p. 369-379.
59. R. G. Castro, R. W. Smith, A. D. Rollett, and P. W. Stanek, *Scripta Metall.*, 26 (1992) 207-212.
60. R. K. Wade and J. J. Petrovic, *J. Am. Ceram. Soc.*, 75(11) (1992) 3160-62.
61. J. J. Petrovic and R. E. Honnell, *J. of Mat. Sci.*, 25 (1990) 4453-4456.
62. Y. L. Jeng, J. Wolfenstine, and E. J. Lavernia, *Scripta Metall.*, 28 (1993) 453-458.
63. S. Jayashankar, S. E. Riddle, and M. J. Kaufman, *High Temperature Silicides and Refractory Alloys*, eds. C. L. Briant, J. J. Petrovic, B. P. Bewlay, A. K. Vasudevan, H. A. Lipsitt, 322 (1994) 33-40.
64. J. J. Petrovic, A. K. Bhattacharya, R. E. Honnell, T. E. Mitchell, R. K. Wade, and K. J. McClellan, *Mat. Sci. and Eng.*, A155 (1992) 259-266.
65. G. R. Anstis, P. Chantikul, B. R. Lawn, and D. B. Marshall, *J. Amer. Ceram. Soc.*, 64(9), 533-538 (1981).
66. B. Lawn, A. Evans, D. Marshall, *J. Amer. Ceram. Soc.*, 63(9-10) (1980) 574-581.
67. C. B. Scruby, C. Jones, J. M. Titchmarsh, and H. N. G. Wadley, *Metal Science*, 15 (1981) 241-261.
68. A. G. Evans and M. Linzer, *J. Amer. Ceram. Soc.*, 56 (1973) 575-80.
69. E. M. Schulson, *Res. Mech. Lett.*, 1 (1981) 111.
70. D. J. Gaydos, R. W. Jech, and R. H. Titran, *J. Mat. Sci. Lett.*, 4 (1985) 138.
71. A. Stergiou and P. Tsakirooulos, *Mat. Res. Soc. Symp. Proc.*, High Temperature Ordered Alloys VI, Eds. J. A. Horton, I. Baker, S. Hanada, R. D. Noebe, D. S. Schwartz, Vol. 364, 911-916 (1995).
72. A. Newman, S. Sampath, and H. Herman, *TMS Proceedings, Processing and Design Issues in High Temperature Materials*, May 1996, Davos, Switzerland, in press.
73. S. Chin, D. L. Anton, and A. F. Giamei, *Microstructure And Mechanical Properties Of Nitrided Molybdenum Silicide Coatings in High Temperature Silicides and Refractory Alloys*, eds. C. L. Briant, J. J. Petrovic, B. P. Bewlay, A. K. Vasudevan, H. A. Lipsitt, 322, 423-429 (1994).
74. D. L. Davidson and A. Bose, *Microstructure And Mechanical Properties Of Nitrided Molybdenum Silicide Coatings in High Temperature Silicides and Refractory Alloys*, eds. C. L. Briant, J. J. Petrovic, B. P. Bewlay, A. K. Vasudevan, H. A. Lipsitt, 322, 431-436 (1994).
75. S. Jayashankar, S. E. Riddle, and M. J. Kaufman, *Microstructure And Mechanical Properties Of Nitrided Molybdenum Silicide Coatings in High Temperature Silicides and Refractory Alloys*, eds. C. L. Briant, J. J. Petrovic, B. P. Bewlay, A. K. Vasudevan, H. A. Lipsitt, 322, 33-40 (1994).
76. A. G. Evans and E. A. Charles, *J. Am. Ceram. Soc.*, 59(7-8), 371-372 (1976).
77. K. T. Faber and A. G. Evans, *Acta Met.*, 31(4), 577-584 (1983).
78. A. G. Evans, *Acta Met.*, 26, 1845-1853 (1978).

# REPORT DOCUMENTATION PAGE

Form Approved  
OMB No. 0704-0188

Public reporting burden for this collection of information is estimated to average 1 hour per response, including the time for reviewing instructions, searching existing data sources, gathering and maintaining the data needed, and completing and reviewing the collection of information. Send comments regarding this burden estimate or any other aspect of this collection of information, including suggestions for reducing this burden, to Washington Headquarters Services, Directorate for Information Operations and Reports, 1215 Jefferson Davis Highway, Suite 1204, Arlington, VA 22202-4302, and to the Office of Management and Budget, Paperwork Reduction Project (0704-0188), Washington, DC 20503.

1. AGENCY USE ONLY (Leave blank)

2. REPORT DATE

3. REPORT TYPE AND DATES COVERED

Final 3/1/94-3/1/97

4. TITLE AND SUBTITLE

Feasibility for improving ambient temperature toughness of mosi2 composites

5. FUNDING NUMBERS

6. AUTHOR(S)

Dr. Sanjay Sampath  
Dr. Herbert Herman

7. PERFORMING ORGANIZATION NAME(S) AND ADDRESS(ES)

State University of New York  
Stony Brook, NY 11794

8. PERFORMING ORGANIZATION  
REPORT NUMBER

9. SPONSORING/MONITORING AGENCY NAME(S) AND ADDRESS(ES)

US Navy Office of Naval Research  
800 N. Quincy Street  
Arlington, VA 22217-5000

10. SPONSORING/MONITORING  
AGENCY REPORT NUMBER

N000149410553

11. SUPPLEMENTARY NOTES

12a. DISTRIBUTION / AVAILABILITY STATEMENT

12b. DISTRIBUTION CODE

13. ABSTRACT (Maximum 200 words)

Due to its high melting point and oxidation resistance, molybdenum disilicide ( $\text{MoSi}_2$ ) is a candidate for high temperature structural components. However, in order for  $\text{MoSi}_2$  to be applicable for these applications, the high temperature creep resistance and low temperature fracture toughness of the compound need to be substantially improved. In this ONR-sponsored study, we are examining the effects of processing on the resulting microstructure and properties of reinforced and unreinforced  $\text{MoSi}_2$ . Samples have been obtained from several laboratories with the goal of determining the effects of purity and processing. The results indicate that a finer grain size in combination with the addition of small particles, whether silica,  $\text{SiC}$ , or precipitates, contributes to the improvement in the material's low temperature fracture toughness.

14. SUBJECT TERMS

15. NUMBER OF PAGES

16. PRICE CODE

17. SECURITY CLASSIFICATION  
OF REPORT

18. SECURITY CLASSIFICATION  
OF THIS PAGE

19. SECURITY CLASSIFICATION  
OF ABSTRACT

20. LIMITATION OF ABSTRACT